Photocatalytic bioheteronanostructures by integrating multicomponent Cu$_2$O–Au nanoparticles into ZnO-coated butterfly wings colored by photonic nanoarchitectures

Gábor Piszter[1,*] , Krisztián Kertész[1], Gergely Nagy[2], Dávid Kovács[1], Dániel Zámbó[1], Zsófia Baji[1], József Sándor Pap[2], and László Péter Biró[1]

[1] *HUN-REN Centre for Energy Research, Institute of Technical Physics and Materials Science, Konkoly-Thege Miklós út 29-33, Budapest 1121, Hungary*
[2] *HUN-REN Centre for Energy Research, Institute for Energy Security and Environmental Safety, Surface Chemistry and Catalysis Department, Konkoly-Thege Miklós út 29-33, Budapest 1121, Hungary*

ABSTRACT

Complex biological photocatalytic heteronanostructures were produced by the integration of different multicomponent Au–Cu$_2$O nanoparticles (NPs) into the blue-colored photonic nanoarchitectures occurring in the wings of male *Polyommatus icarus* butterflies. Both bare wings and wings conformally coated by 15-nm ZnO by atomic layer deposition were used as substrates. The NPs were characterized by UV–visible spectroscopy, focus stacking optical microscopy, and electron microscopy. After the deposition of the different NPs, the photocatalytic performance of the samples under visible light illumination was tested by the photodegradation of methyl orange in aqueous solution monitored continuously by an immersion probe. It was found that the components of the biological hetero-nanoarchitecture: ZnO-coated wings and wings without ZnO with deposited NPs exhibited poor catalytic performance. But the combined system: ZnO-coated wings with NPs deposited onto them exhibited sixfold to eightfold increase in their catalytic performance. This increase is attributed to the extension of the ZnO absorption into the visible range and to the formation of the heterojunction between the n-type ZnO and the p-type Cu$_2$O NPs which resulted in the charge transfer of the photogenerated carriers. As the samples exhibited good stability under the continuous magnetic stirring, they can be used in flow-through systems suitable for wastewater remediation. The biological templates for the hetero-nanoarchitectures were produced by the controlled breeding of herbivorous insects, which does not raise any environmental concerns.

🙋 Springer

Introduction

Inorganic and organic hybrids are a class of new materials that are purposely designed and arranged at constituting material levels (often at nanoscale) to provide new morphological attributes and properties [1]. Hybrid nanomaterials may exhibit novel properties and/or enhanced performance—different from their constituents—due to the combined effects of small size and large specific surface of the nanoparticles (NPs), interfaces, and interactions between nanoparticles/nanostructures and matrices [2].

The concept of biocomposites is evolving to include nanostructured hybrid materials, too. Biopolymers, such as cellulose and chitin, are plentiful in nature and are both renewable and biodegradable, making them viable alternatives to petroleum-derived plastics [3]. Moreover, many organisms developed intricate nanoarchitectures from chitin and cellulose to fulfill important biological functions [4]. A particularly interesting class of these nanoarchitectures are the photonic nanoarchitectures built of chitin in the wing scales of many butterfly species possessing structural coloration [5–10]. In the past decades, various methods have been developed to reproduce photonic nanoarchitectures of biologic origin [4]. Unfortunately, most of these methods are technically demanding, costly, time consuming, and some of the used materials cannot be regarded as environmentally friendly.

The quickly developing biocomposite industry has recently drawn great attention to diverse applications, from household articles to automobiles. This is owing primarily to their low cost, being biodegradable and lightweight, available, and environmental concerns over synthetic and non-renewable materials derived from limited resources, like fossil fuel [11]. The larvae of most butterfly and moth species—like the well-known, domesticated *Bombyx mori*, the cocoons of which are the source of the natural silk fiber [12]—are herbivorous, so that they can be reared and mass produced without environmental concerns [12, 13]. The photonic nanoarchitectures in the wings of butterflies possessing structural color may constitute an advantageous platform both under the aspect of cost and environmental safety for applications demanding large areas of stable photonic nanoarchitecture, for enhanced photocatalytic [14] or high-sensitivity surface-enhanced Raman spectroscopy (SERS) [15] applications.

Among other opportunities offered by photonic crystals (PhC), the exploitation of slow light effects for the enhancement of photocatalytic efficiency is very promising [16, 17]. Recently, several groups reported butterfly wings possessing structural color generated by PhC-type nanoarchitectures as biotemplates for the conformal deposition of thin layers of photocatalytic materials, like ZnO [18, 19]. Bioinspired plasmonic photocatalysts are also in the focus of attention for solar energy conversion and energy storage [20]. Evolution has already taken advantage of solar energy for billions of years; plants, algae, and even some bacteria can efficiently use sunlight via photosynthesis. A large variety of photocatalysts has been developed to convert solar energy for various applications [21–23].

A major obstacle in further improving photocatalytic semiconductors such as ZnO and Ti_2O is their large bandgap that allows only UV light excitation. When using biotemplated Ti_2O [24] or ZnO [14, 25] photocatalytic layers on butterfly wings, increased efficiency in the visible spectral range was reported. If a more complex approach is adopted for the tuning of the reflectance maximum of such photonic biotemplated heteronanostructures, to overlap with the absorption maximum of the pollutant to be eliminated [26], further increase in the photocatalytic efficiency can be achieved [27].

In the present work, for the first time, a systematic study is reported on biotemplated heteronanostructures produced by coating blue-colored male *Polyommatus icarus* butterfly wings using ZnO and depositing hybrid NPs from the Cu_2O–Au heteronanostructures family. The resulting composite material is designed to enhance the efficiency in using the visible part of the solar spectrum. The effect of various NPs (Cu_2O octahedra, Cu_2O octahedra with Au nanograins grown on their facets, Cu_2O octahedra with a centrally incorporated Au nanorod, and spherical Au NPs) was tested. This family of strictly size-regulated NPs has been selected because earlier results showed that Au doping of the Cu_2O NPs can significantly enhance their photocatalytic efficiency [28, 29]. Moreover, the Cu_2O-based nanocomposites are intensely investigated for enhancing the photocatalytic efficiency of Ti_2O and ZnO under visible light illumination for environmental protection [29–35]. Cu_2O has the advantage of being abundant, environmentally safe, and minute amounts of Au can be efficiently used to tune its properties [32, 36–38]. Au decoration of the Cu_2O NPs can enhance

their structural stability even during long-time light exposure in aqueous environment [28].

When aiming at environmental protection applications, and water remediation in particular, the immobilization of the NPs on an appropriate substrate is of great importance [39]. Due to their complex hierarchical structure from tens of nanometers to centimeters, butterfly wings are particularly well suited for this purpose. An important question is to what extent and in which ways the properties of the complex, hybrid photocatalytic NPs are affected by the interaction with such substrates. The Cu_2O NPs are known to be Mie resonators, for which the substrate can have important effects [40–42].

We used butterfly wing-based substrate (i) to immobilize the NPs, (ii) to provide increased contact surface between the solute and the photocatalytic surface, and (iii) to exploit structural complexity by using the hierarchical nanoarchitecture. The chemical and plasmonic complexity are provided by the conformal ZnO thin film, and the deposited NPs used for doping [25]. We performed a set of systematic experiments to test the optical characteristics and photocatalytic performance of the blue wings of male *P. icarus* butterflies in the degradation of methyl orange (MO) using visible light. Samples with or without 15-nm-thick conformal ZnO coating under the hybrid NPs [29, 43] have been compared. We found that the heterojunction between the n-type ZnO and the p-type Cu_2O NPs dominated the photocatalytic process and produced a sixfold to eightfold improvement of the photocatalytic MO decomposition rates compared to the performance of homolog samples without ZnO coating under identical experimental conditions.

Materials and methods

Butterfly wings

The butterfly species *P. icarus* is dimorphic: The dorsal wing surface of the females is dominantly brown, while the males' are uniformly blue [13]. The blue color of the males is generated by PhC-type photonic nanoarchitectures constituted of chitin and air [44]. The color and the structure are remarkably constant in natural populations [45] with a 20-nm difference in the main reflectance peak position between European and Asian populations. If reared under controlled conditions in the laboratory, a full egg-imagine cycle

has last about 2 months, and a single female may lay 500–700 eggs [13], half are males the wings of which can be used. The experiments were conducted using the dorsal blue surface of 80 wing samples. To demonstrate color consistency, the individual spectra, the averaged spectrum, and standard deviations are given in Fig. S1a.

Atomic layer deposition (ALD)

The conformal, 15-nm-thick ZnO layer was deposited by atomic layer deposition in a Picosun Sunale R-100 reactor. This is a flow-type ALD reactor with 5N purity nitrogen as a carrier and purging gas. The ZnO precursors were electronic grade purity diethylzinc from Strem Chemicals Inc. and > 17.5 MΩcm deionized water. The 15-nm-thick ZnO layers were deposited as 90 ALD cycles, with one cycle consisting of 0.5-s precursor pulse, 15-s purge, 0.5-s water pulse, and 20-s nitrogen purge. This process is appropriate to coat the high aspect ratio structures of the butterfly wings. The deposition took place at 100 °C which is high enough for the growth of the good quality oxide layer, but low enough not to harm the sensitive organic structures.

Nanoparticle preparation

The Cu_2O-based hybrid NPs were prepared in such a way that the size and shape of the Cu_2O NPs were the same (Fig. 1) using a methodology reported in detail earlier [29]. Cu_2O NPs with octahedral shape were synthesized in aqueous medium, and their solvent was exchanged to anhydrous ethanol to extend their shelf-life and to avoid overoxidation. Small Au nanograins were deposited onto these octahedra in a one-pot synthesis. As its counterpart, octahedral Cu_2O shell was grown onto Au nanorod seeds by keeping the shape, size, and the Cu:Au atomic ratio identical. The Cu_2O-type NPs were deposited from ethanol-based sols. The Au NPs were produced by the traditional Turkevich method [46, 47] and were deposited from water-based sols. When (Cu_2O + Au) samples were prepared, first, the ethanol-based Cu_2O sol was added, followed by the water-based sol of Au NPs. When only Au NPs were used, a droplet of ethanol was used to wet the butterfly wing prior to the deposition. The optical properties of the NPs in sol were characterized by extinction measurements using a Shimadzu UV3600i UV–Vis–NIR spectrophotometer in quartz cuvette. The concentration of the solutions
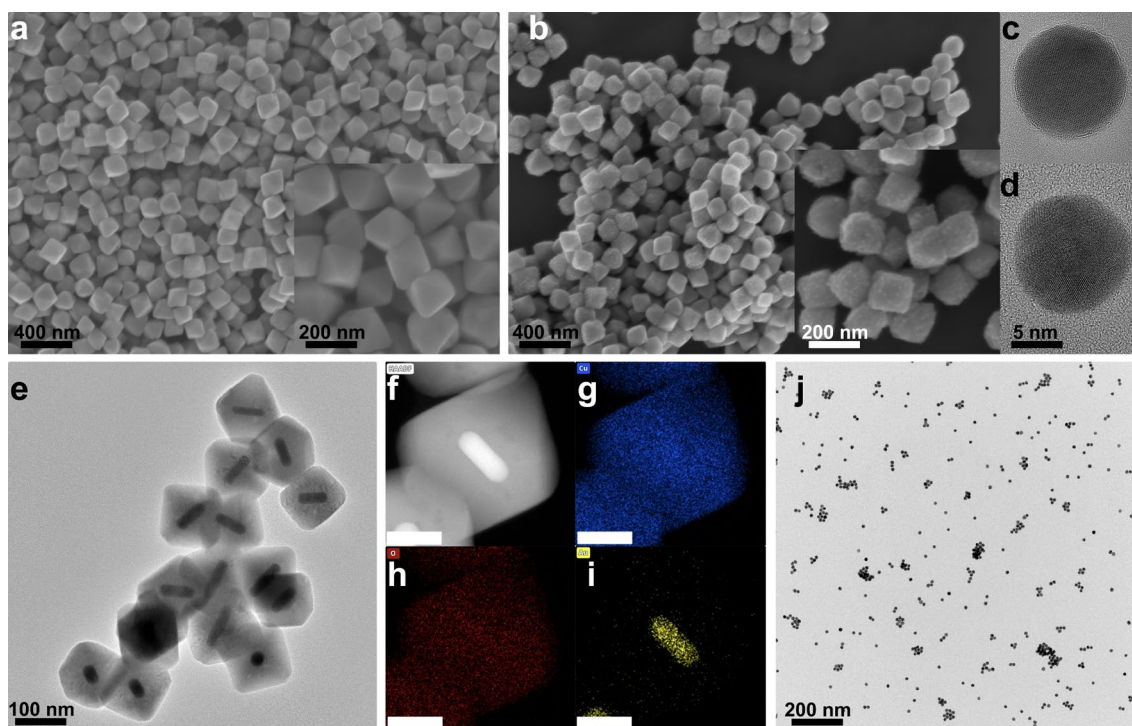
Figure 1 Morphology of the used NPs: **a** SEM image of Cu$_2$O NPs, note in the right lower corner inset the smooth surface of the (111) facets; **b** SEM image of Au@Cu$_2$O NPs, note in the right lower corner inset the rough surface of the facets due to the Au nanograins grown on the Cu$_2$O NPs; **c** and **d** two Au NPs shown in high-resolution TEM images; **e** TEM image of AuR@Cu$_2$O NPs, note the contrast difference due to the Au nanorod inside the Cu$_2$O octahedra; **f** HAADF image; **g** Cu, **h** O, and **i** Au distribution of a AuR@Cu$_2$O NP measured with EDS, scale bars: 5 nm; and **j** TEM image of spherical Au NPs.

was determined by total reflection X-ray fluorescence (TXRF) analysis for Cu$_2$O, Au@Cu$_2$O, and AuR@Cu$_2$O samples, while the Au^0 concentration of the Au NP solution was calculated based on the extinction value at 400 nm [48]. The final concentration of the Cu$_2$O in all particle solutions was set to 0.045 mg/ml. Au concentration was set to 0.015 mM to ensure the same Cu$_2$O:Au ratio in the heteroparticle and mixed samples. The morphology and the composition of the used NPs was characterized by SEM and TEM including elemental analysis by energy-dispersive X-ray spectroscopy (EDS).

Sample preparation

The wings were removed from the body of the butterflies and were fixed onto glass substrates cut from microscope slides using PMMA photoresist as adhesive. The glass-mounted wings were subjected to an ethanol treatment (soaking the samples in ethanol for 6 h at 50 °C, ETA50) to remove the native wax layer covering the wing scales (Fig. S1b) [49].

The pristine wings after the wax removal treatment (ETA50) and the wing samples with the 15-nm ZnO layer were completely encapsulated into glass after the ZnO deposition in such a way that only the circular area of 8 mm in diameter was left to interact with the test solution during dye degradation measurements. From both uncoated wing samples and wings which were coated by 15-nm ZnO prior to the NP deposition, a full set of samples was prepared to which an additional of 5-nm ZnO layer was deposited, to improve the fixing of the NPs on the substrate and to improve the electrical contact between the ZnO layer and the NPs. When performing the post-NP deposition of 5-nm ZnO coating, the upper glass slides with the 8-mm diameter holes were protected from the ZnO using polyimide tape (Kapton Tape, DuPont Inc., Wilmington, DE, USA) which was removed after the deposition. In this way, the post-deposition of 5-nm ZnO affected only the wings exposed through the 8-mm diameter opening of the glass covers.

After the removal of the wax and ZnO deposition, PDMS rings with an inner circular hole of 8 mm in

diameter (Silicone sealing ring f. GL threads, without PTFE washer, 16 × 8 mm, DWK Life Sciences, Germany) were pressed mechanically onto the wing/substrate, to avoid the uncontrolled spreading of the NP sol used to deposit the NPs. Four types of NP sols were used: Cu_2O octahedra (Cu_2O), Cu_2O octahedra with Au nanograins grown on their facets (Au@Cu_2O), Cu_2O octahedra with a centrally incorporated Au nanorod (AuR@Cu_2O), and spherical Au NPs (Au). The sols were prepared in such a way that by unit volume, they contained the same amount of Cu_2O—if containing Cu_2O—and of Au—if containing Au. Except for the sequentially deposited (Cu_2O + Au) samples, 120-µl sol was deposited into the PDMS ring for all samples. For the (Cu_2O + Au) samples, for each added species, 120-µl sol was used to achieve the same Au/Cu_2O ratio as for the Au@Cu_2O and AuR@Cu_2O samples.

Reflectance spectrophotometry

The reflectance and transmittance measurements were carried out using an Avantes (Avantes BV, Apeldoorn, The Netherlands) modular fiber-optic spectrophotometer (AvaSpec-HSC1024 × 58TEC-EVO) with stabilized deuterium–halogen light source (AvaLight-DH-S-BAL) and fiber-optic accessories. When butterfly wing-based samples were measured, an Avantes WS-2 white standard tile was used as a reference. When samples were prepared on clean glass substrates—using the same PDMS rings, and the same amounts of sols as for the butterfly wings—to allow the measurement of the reflectance and transmittance of the NPs in dry state, the reflectance and transmittance measured on the clean glass was used from the close vicinity of deposited NPs as a reference.

Photocatalytic dye degradation

Dye degradation experiments were carried out in a glass cuvette with continuous magnetic stirring. Visible light illumination was supplied by a 300-W Xe lamp with infrared filter and fiber optics (Asahi Co., MAX-303). For the experiments, quasi-stationary conditions were set: i.e., the area of the active photocatalytic surface was kept at a low value (0.52 cm^2) on purpose if compared to the total volume of the MO test solution ($c = 50$ µM, 20 cm^3). This provided quasi-stationary reaction conditions during the photocatalytic experiment with respect to the dye concentration and allowed unbiased determination of the initial reaction rates at relative low conversion values. The change in MO concentration was followed by UV–visible spectrophotometry (Agilent Cary 60 spectrophotometer equipped with an immersion probe of 1-cm path length), by measuring the absorption maximum at 463 nm with 5-min intervals. From the absorbance, the conversion was calculated and plotted as $100(I_0 - I)/I_0$ (%), where I_0 is the initial absorption intensity, and I is the intensity at the time of the measured data point.

Results

The various NPs used from the Cu_2O-Au family were characterized morphologically by SEM and TEM, and their composition was confirmed by EDS (Fig. 1). Four types of NPs have been used to decorate the wing substrates: octahedral Cu_2O (Cu_2O), octahedral Cu_2O with Au nanorod in its center (AuR@Cu_2O), octahedral Cu_2O decorated with small Au nanograins on the facets (Au@Cu_2O), and small Au nanospheres without the Cu_2O carrier (Au). The size of the Cu_2O NPs is in the range of 136 ± 12 nm in terms of base edge length. The Au nanograins in the Au@Cu_2O NPs have an average size of 6.8 ± 1.4 nm. The base edge length of the AuR@Cu_2O NPs was 137 ± 11 nm [29]. The Au NPs used have spherical shape and diameter in the range of 15–20 nm. The concentration of the Au NP sol was fixed at such a value that 120-µl sol contains the same amount of Au as 120 µl of Au@Cu_2O and AuR@Cu_2O sols.

The extinction of the NPs in the sols was measured by UV–visible spectroscopy (Fig. 2). By comparing the normalized curves, one may observe that the extinction of the mixed (Cu_2O + Au) sol with a composition of 50:50 does not differ significantly from that of the Cu_2O. This is not surprising as the concentration of Au NPs is much smaller than that of the Cu_2O NPs. On the other hand, when Au nanograins are used to decorate the Cu_2O NPs (Au@Cu_2O) or Au rods are located in the center of the Cu_2O octahedra (AuR@Cu_2O), more pronounced effects can be identified. The surface decoration causes a moderate increase in the extinction from 550 to 1000 nm, while the presence of the AuR in the center of the octahedra induced extra peaks in the range of 640–700 nm.

In Fig. 3, the transmittance of the different NP samples prepared by drop-casting 120-µl sol onto glass substrates using PDMS rings is shown. The only exception is the (Cu_2O + Au) sample for which 120 µl

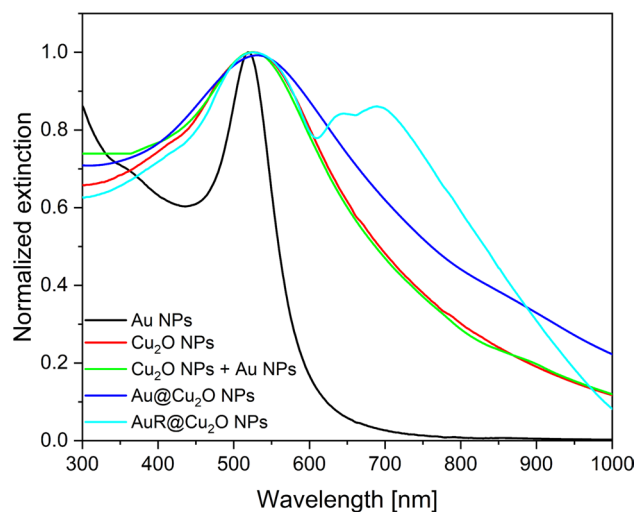**Figure 2** Normalized extinction spectra of the investigated NP sols.

ethanol $n = 1.36$) and to clustering, and the corresponding interparticle plasmon coupling [51].

The transmittance of Cu_2O NPs on glass and of the $Au@Cu_2O$ NPs on glass (Fig. 3a) shows characteristic differences in the spectral range from 350 to 800 nm. One may observe that the two spectra are shifted vertically with respect to each other, in such a way that the transmittance of the $Au@Cu_2O$ sample is lower. The transmittance of the ($Cu_2O + Au$) sample is close to that of the $Au@Cu_2O$ sample in the spectral range between 350 and 475 nm. The transmittance of the ($Cu_2O + Au$) sample crosses the $Au@Cu_2O$ sample transmittance in the spectral range from 475 to 600 nm—where the LSPR band of the Au NPs is found—and runs close to the curve corresponding to the Cu_2O sample at 800 nm.

In Fig. 3b, the relative transmittance of Au NPs on glass, Cu_2O NPs on glass, and $AuR@Cu_2O$ NPs on glass is compared. From 300 to 475 nm, the curves corresponding to Cu_2O and $AuR@Cu_2O$ run in parallel. The difference starts to build from 475 nm and reaches the greatest magnitude in the range from 600 to 700 nm. The diameter of the Au rod (25.7 ± 1.8 nm) [29] in the center of the Cu_2O octahedra is comparable with the size of Au NPs (Fig. 1), so it is not surprising that the differences between the two curves become noticeable in the same spectral range where the ($Cu_2O + Au$) sample started to deviate from the Cu_2O sample (Fig. 3a). The most important difference in the range of 600–700 nm was attributed to the transversal plasmon resonance of the Au rod and its interaction
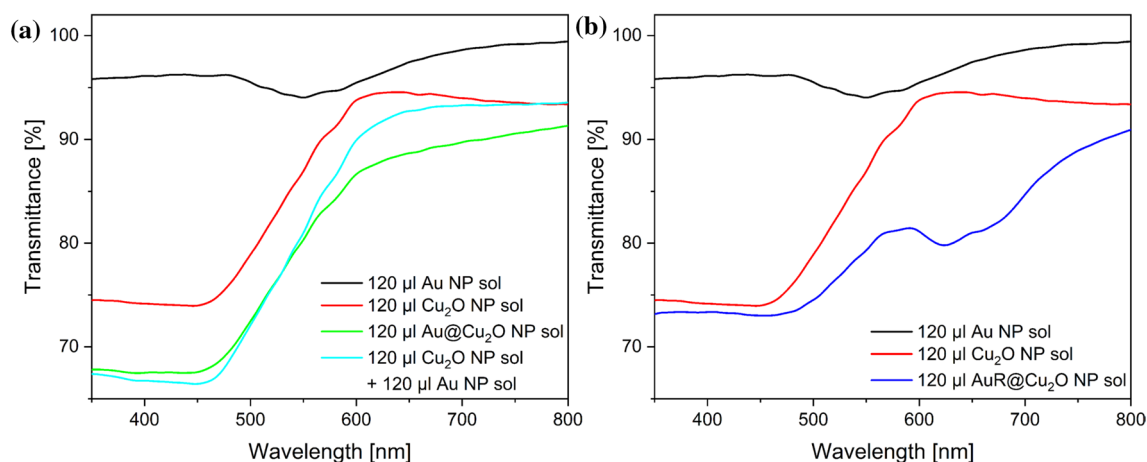
was used from each sol. For more clarity, Fig. 3 is presented with two panels: In Fig. 3a, the relative transmittance of samples with Au NPs, Cu_2O NPs, $Au@Cu_2O$ NPs, and ($Cu_2O + Au$) NPs on glass is compared. The surface plasmon resonance peak of the Au NPs is located at 550 nm. This value is redshifted by 30 nm with respect to the value measured in the aqueous Au NP sol and also broadens remarkably. As the decrease in the refractive index of the medium (for air $n = 1$) is expected to cause blueshift in plasmon resonance [50], the observed redshift is attributed to the presence of the glass substrate ($n = 1.52$ as compared to that of

Figure 3 Relative transmittance of 120-μl NP sols from the Cu_2O–Au family. **a** Au, Cu_2O, and ($Cu_2O + Au$) are shown. **b** Au, Cu_2O, and $AuR@Cu_2O$ are shown. The sols were drop-casted onto glass substrates, and the transmittance of clean glass substrate was taken as a reference.

with Cu_2O [29]. This absorption causes that the AuR@ Cu_2O sol does not exhibit orange coloration like the Cu_2O sol, but grayish–green color (see Fig. S2c in ref. [29]).

The modification of the color of butterfly wings is presented in Fig. 4. The curves are an average of reflectance values measured on 40 individual wings subjected to the same treatment. The ETA50 treatment for wax removal causes the amplitude increment of the blue reflectance maximum and also causes a moderate blueshift in the peak wavelength. The deposition of the conformal ZnO layer of 15-nm thickness, as reported earlier [10, 14], causes the redshift of the reflectance maximum and is associated with a moderate decrease in the reflectance amplitude obtained after the ETA50 treatment. After the deposition of the conformal 15-nm ZnO, the wings very clearly show the absorption edge of the ZnO layer at 380 nm, at wavelengths smaller than this value no features can be observed on the reflectance spectra.

As a general rule, the deposition of the NPs on the wings produces redshift of the reflectance maxima (Figs. 5 and 6). For ease of comparison, the absorbance of MO was also plotted. The peak wavelength of the wing reflectance obtained after the NP deposition depends on the presence/absence of the conformal ZnO coating (Table 1).
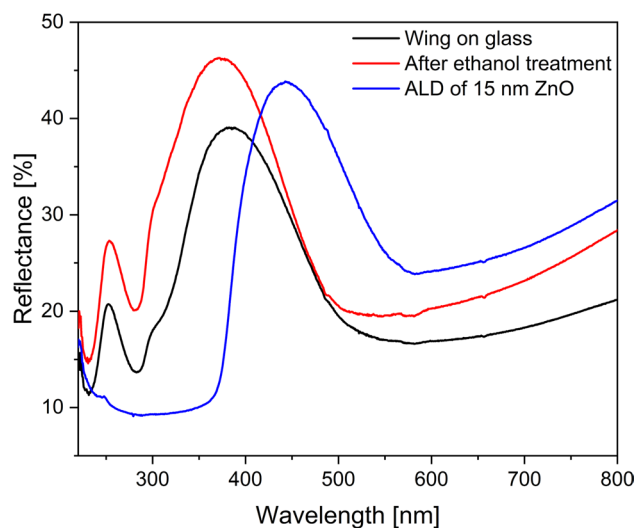

Figure 4 Averaged reflectance of 40 butterfly wings fixed onto glass substrates (black), the wings after being subjected to 50 °C ethanol treatment (red), and after the deposition of 15 nm of conformal ZnO layer was carried out by ALD (blue).

In Fig. 5, one may observe that the spectral modifications can be organized in three groups: (i) the Au NPs—as their concentration is very low as compared to the Cu_2O—produce only a slight redshift (19 nm) and almost no change (0.3%) in the amplitude of the reflectance maximum; (ii) the Cu_2O, the Au@Cu_2O, and the AuR@Cu_2O group produce comparable redshift (40–41 nm) and amplitude decrease (12–13%) which can be attributed mainly to the Cu_2O, as the major constituent of the NPs; and (iii) the (Cu_2O + Au) NPs cause a smaller decrease in the amplitude of the reflectance maximum (32 nm) and smaller redshift (8%) of the reflectance peak as compared to group (ii) (Table 1).

In Fig. 6, the spectral modifications produced by the deposited NPs on the butterfly wings conformally coated by 15-nm ZnO are shown. Two groups can be identified based on the spectral changes: (i) Au and AuR@Cu_2O NPs produce a redshift of 14–15 nm associated with an amplitude decrease of 2.5–5.5%; (ii) the Cu_2O, Au@Cu_2O, and the (Cu_2O + Au) NPs cause a redshift of 34–39 nm with an amplitude decrease of 11–14% (Table 1).

In Fig. S2, the relative reflectance of the wing samples after the NP deposition with respect to the reflectance measured before the NP deposition is compared. In Fig. S2a, corresponding to the uncoated wings, all the NPs caused a reduction of the reflectance in the range of 250–400 nm and an increase in the reflectance in 475–550 nm. Figure 3 shows that from the short-wavelength side to about 445 nm all the used NPs reduce light transmission without important wavelength dependence. It is worth mentioning that the Au@Cu_2O and the (Cu_2O + Au) curves almost overlap from 375 to 800 nm, i.e., in the entire range where the glass cuvette has high transmittance. The AuR@Cu_2O is also not far from these curves; the major difference is the stronger increase in reflectance from 475 to 550 nm as compared with the Au@Cu_2O and the (Cu_2O + Au) curves. Clearly, the relative reflectance corresponding to the Au and the Cu_2O NPs is different from the three curves discussed above.

In Fig. S2b, the relative reflectance corresponding to the wings coated by 15 nm of ZnO is compared. The deposition of the NPs causes a marked decrease in the reflectance in the range of 380–530 nm and a moderate increase in the reflectance in the range of 530–800 nm. The magnitude of the reflectance decrease separates Au and AuR@Cu_2O samples from the other three types of samples. These observations are in good agreement
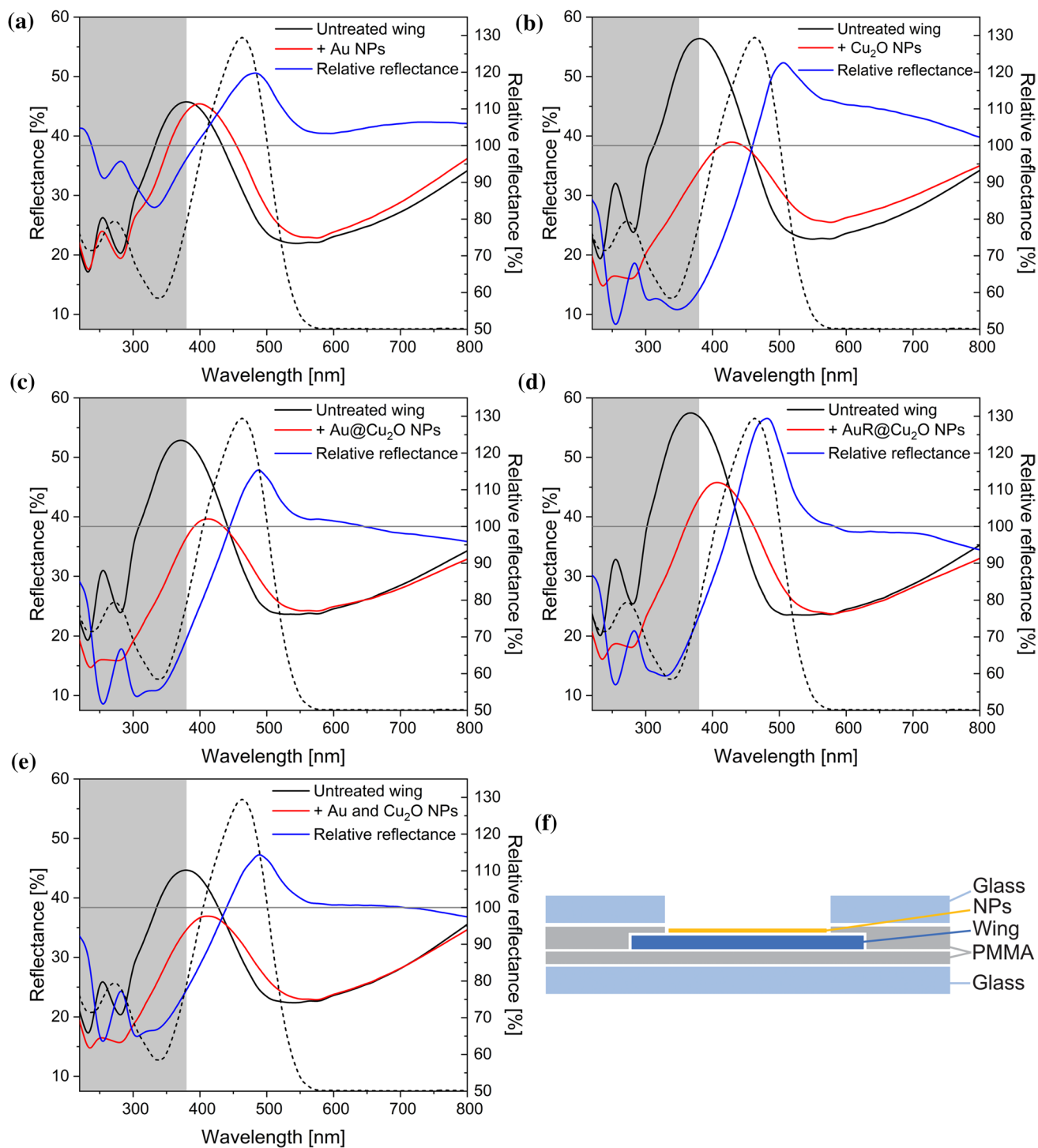
Figure 5 The effect of NPs on the reflectance of ethanol pre-treated butterfly wings, using **a** 120 μl sol of Au, **b** Cu₂O, **c** Au@Cu₂O, **d** AuR@Cu₂O, and **e** 120 μl of Au NP sol + 120 μl of Cu₂O sol for deposition. The averages of spectra measured on three different wings are shown before (black) and after (red) NP deposition, and relative reflectance of the deposited samples with respect to the initial state of the wings (blue). The gray shading marks the spectral region in which the transmission of the glass cuvette used for photocatalytic measurements decreased to zero. The normalized absorbance of the MO dye is plotted with dashed black lines in each panel. Note that after the NP deposition, all reflectance maxima were shifted toward the transmittance window of the glass cuvette. In **f**, the schematic sample structure is shown (dimensions not to scale).

Figure 6 The effect of NPs on the reflectance of butterfly wings coated with 15-nm conformal ZnO, using **a** 120-μl sol of Au, **b** Cu$_2$O, **c** Au@Cu$_2$O, **d** AuR@Cu$_2$O, and **e** 120 μl of Au NP sol + 120 μl of Cu$_2$O sol for deposition. The averages of spectra measured on three different wings are shown before (black) and after (red) NP deposition, and relative reflectance of the deposited samples with respect to the initial state of the wings (blue). The gray shading marks the spectral region in which the transmittance of the glass cuvette used for photocatalytic measurements decreased to zero. The normalized absorbance of the MO dye is plotted with dashed black lines in each panel. Note that after the NP deposition, all reflectance maxima were shifted toward the transmittance window of the glass cuvette. In **f**, the schematic sample structure is shown (dimensions not to scale).
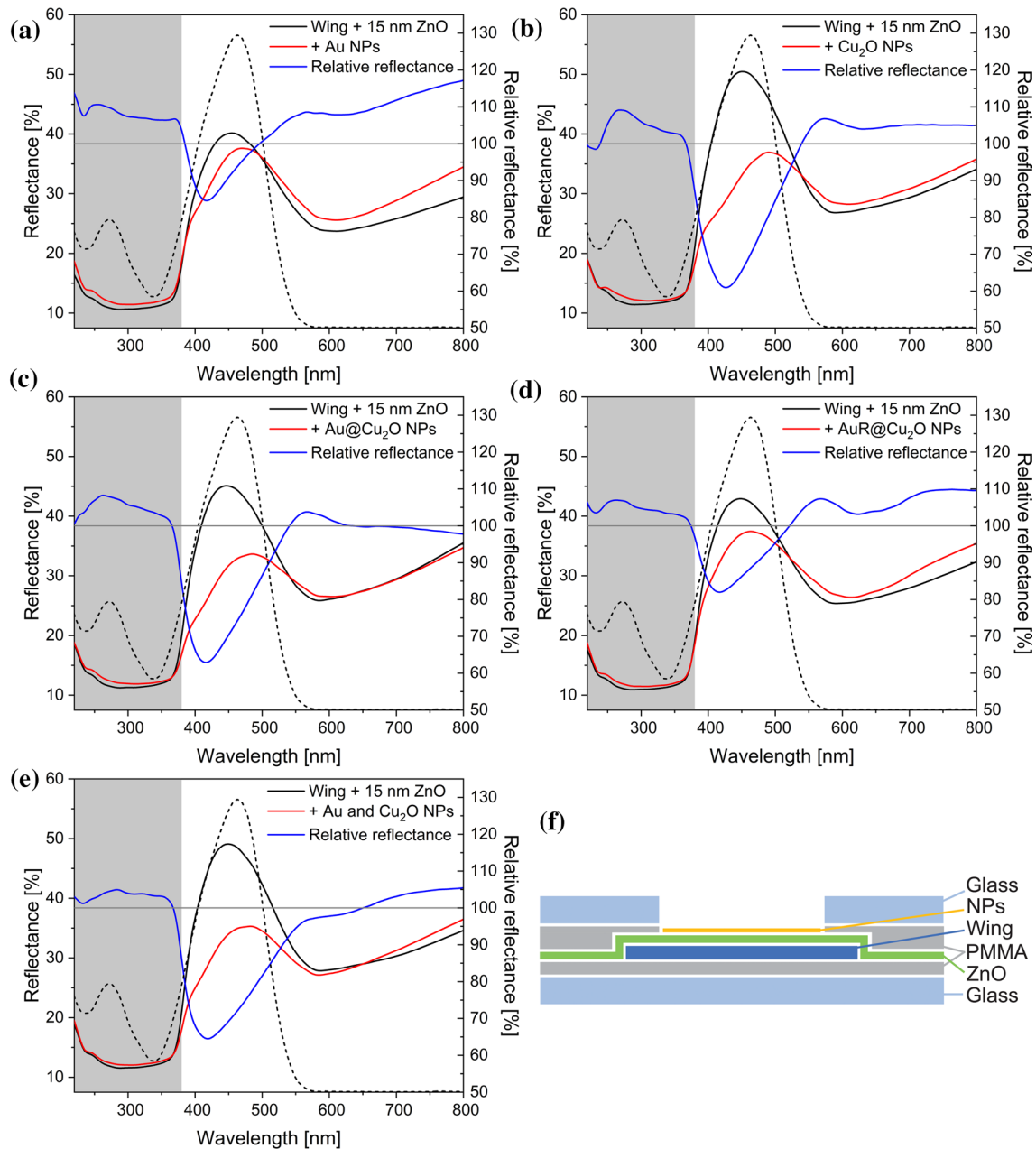
with the optical microscopy data of the NP-deposited wings acquired with a focus stacking optical microscope (Fig. S3). These images cannot show individual NPs, but clusters are clearly visible, and the clustering is affected by the surface chemistry of the substrate and the kind of deposited NPs.

The deposition of 5 nm of ZnO following the NP deposition has only a minor effect on the optical

Table 1 Peak wavelength (nm) and amplitude (%) of the reflectance maxima, before and after the deposition of the various NPs onto butterfly wings uncoated or coated with 15-nm ZnO

Coating	Deposited NPs	Before (nm)	Before (%)	After (nm)	After (%)	Δ (nm)	Δ (%)
Uncoated	Au	379.86	45.74	399.28	45.42	19.42	− 0.32
Uncoated	Cu_2O	380.64	56.39	428.75	38.97	48.11	− 17.42
Uncoated	$Au@Cu_2O$	371.31	52.86	412.47	39.64	41.16	− 13.22
Uncoated	$AuR@Cu_2O$	366.64	57.47	407.04	45.78	40.4	− 11.69
Uncoated	$(Cu_2O + Au)$	379.08	44.67	410.92	36.94	31.84	− 7.73
15-nm ZnO	Au	455.05	40.16	469.72	37.61	14.67	− 2.55
15-nm ZnO	Cu_2O	451.18	50.46	490.55	36.93	39.37	− 13.53
15-nm ZnO	$Au@Cu_2O$	446.54	45.08	485.15	33.65	38.61	− 11.43
15-nm ZnO	$AuR@Cu_2O$	448.09	42.92	463.55	37.45	15.46	− 5.47
15-nm ZnO	$(Cu_2O + Au)$	448.86	49.08	482.84	35.29	33.98	− 13.79

properties of the wings, shown in Figs. S4 and S5. As a general trend, a slight increase in the reflectance can be observed in the spectral range of 450–800 nm for the uncoated wings and 550–800 nm for the wings with 15-nm ZnO. There are two moderate exceptions: The samples with Au NPs show no increase in reflectance. In contrast, the largest increase, of about 10%, is observed for the $(Cu_2O + Au)$ samples, irrespective of the 15-nm ZnO coating of the wings. This behavior can be tentatively associated with the improved electrical contacts between the nearby Cu_2O and Au NPs which after the NP deposition were not in contact, and the post-deposition of 5-nm ZnO helped in establishing electrical contacts between the NPs. It was shown experimentally that the decay of photoexcited electron–hole pairs into localized surface plasmons (LSPs) dramatically modifies the Au emission wavelength, line shape, and quantum efficiency depending both on particles size and separation [52]. Under visible light irradiation in the $ZnO@Au@Cu_2O$ system, both Cu_2O and ZnO transfer electrons toward the Au [53]. The measurements are carried out with an integrating sphere, so the reduction of scattering cannot be the cause of the increased reflectance. To a lesser extent, a similar increase in the reflectance of the $Au@Cu_2O$ sample is present after the post-deposition of 5-nm ZnO, too (Figs. S4 and S5).

The photocatalytic performance of all samples was evaluated by the decomposition of MO in aqueous solution in a glass cuvette upon visible light illumination under continuous stirring. The results are given in Table 2 and presented in Fig. 7. Exemplary conversion *vs.* time plots are shown in Fig. S6 (see methodological considerations therein). A number of reference samples described in Table S1 are also included in Fig. 7 to facilitate the interpretation of the data. The reference samples clearly show that the flat glass and the PMMA are inert in the photocatalytic process. The on-purpose roughening of the glass—to improve the adherence of the PMMA to the glass surface—is causing enhancement of the adsorption of MO. The increase in the surface roughness causes the increase in the specific surface available for dye adsorption. On the other hand, it causes no difference if the butterfly wing is fixed onto flat glass or rough glass, as the PMMA adhesive applied for fixing the wings on substrate flatten out the roughness of the glass. As one may expect, the conformal 15-nm ZnO coating produces some increase in the photocatalytic performance, but due to the fact that ZnO absorbs negligibly in the visible, only about 12% of the total light power (Fig. S7), this effect is moderate.

The uncoated wings after the deposition of the NPs have poor photocatalytic activity. A sixfold to eightfold increase in the catalytic performance is observed when the NPs were deposited on butterfly wings with 15-nm conformal coating of ZnO (Fig. 7). Despite some differences in the magnitude of this enhancement, all used NPs generate an increase in this range. With the exception of the $Au@Cu_2O$ NP on the wings deposited with 15-nm ZnO, the conformal post-deposition by 5-nm ZnO does not significantly affect the photocatalytic performance but for certain NPs reduces the standard deviation of the photocatalytic results (Fig. 7).

Table 2 Sample modification details and photocatalytic activity of the fabricated biological heteronanostructures

Sample name[a]	Wing type	Deposited NPs	Post-deposition 5-nm ZnO	Reaction rate (nmol/min)	Standard deviation (nmol/min)
W0-Au	ETA50	Au	No	0.05	0.03
W0-Cu$_2$O	ETA50	Cu$_2$O	No	0.01	0.01
W0-Au@Cu$_2$O	ETA50	Au@Cu$_2$O	No	0.05	0.02
W0-AuR@Cu$_2$O	ETA50	AuR@Cu$_2$O	No	0.03	0.03
W0-(Cu$_2$O + Au)	ETA50	(Cu$_2$O + Au)	No	0.04	0.02
W15-Au	ETA50 + 15-nm ZnO	Au	No	0.40	0.04
W15-Cu$_2$O	ETA50 + 15-nm ZnO	Cu$_2$O	No	0.38	0.09
W15-Au@Cu$_2$O	ETA50 + 15-nm ZnO	Au@Cu$_2$O	No	0.35	0.16
W15-AuR@Cu$_2$O	ETA50 + 15-nm ZnO	AuR@Cu$_2$O	No	0.36	0.10
W15-(Cu$_2$O + Au)	ETA50 + 15-nm ZnO	(Cu$_2$O + Au)	No	0.42	0.03
W0-Au-5	ETA50	Au	Yes	0.05	0.03
W0-Cu$_2$O-5	ETA50	Cu$_2$O	Yes	0.03	0.01
W0-Au@Cu$_2$O-5	ETA50	Au@Cu$_2$O	Yes	0.06	0.03
W0-AuR@Cu$_2$O-5	ETA50	AuR@Cu$_2$O	Yes	0.05	0.03
W0-(Cu$_2$O + Au)-5	ETA50	(Cu$_2$O + Au)	Yes	0.03	0.02
W15-Au-5	ETA50 + 15-nm ZnO	Au	Yes	0.37	0.03
W15-Cu$_2$O-5	ETA50 + 15-nm ZnO	Cu$_2$O	Yes	0.37	0.05
W15-Au@Cu$_2$O-5	ETA50 + 15-nm ZnO	Au@Cu$_2$O	Yes	0.29	0.07
W15-AuR@Cu$_2$O-5	ETA50 + 15-nm ZnO	AuR@Cu$_2$O	Yes	0.35	0.03
W15-(Cu$_2$O + Au)-5	ETA50 + 15-nm ZnO	(Cu$_2$O + Au)	Yes	0.36	0.06

[a]Sample naming: W0 designates ETA50 treatment of the wing, W15 designates 15-nm conformal ZnO coating after the ETA50 treatment, the NP type is indicated after the first dash, and post-deposition coating with a layer of 5-nm ZnO is indicated with -5 ending of the sample name

Discussion

The sixfold to eightfold increase in the photocatalytic performance using only visible light illumination of the biohybrid photonic nanoarchitecture as compared to the performance of the constituents is a very promising result. The more so that the Cu$_2$O used to obtain this increase with respect to the butterfly wings conformally coated with ZnO is also a cheap, abundant, and non-toxic material. The butterfly wings conformally coated by 15 nm of ZnO and decorated with NPs from the Cu$_2$O family, using a simple process of drop-casting the NP sol onto the wings could constitute an attractive biological heteronanocomposite with application possibilities in wastewater remediation. As our experiments were carried out with continuous stirring, the results show (Table 2) that the various NPs adhered well to the coated butterfly wing and were not washed away even after three consecutive experimental runs. So, it is expected that such heteronanocomposites can be used in flow-through systems illuminated by natural sunlight. Our results show that the

visible range of solar light can effectively induce the photodegradation processes in such cheap systems.

The NPs were thoroughly characterized previously in sols regarding both their chemical and physical properties [29]. When using only UV illumination (being off-resonant with the plasmon excitation of the gold, thus, excites excitons only in the semiconductor), the presence and the location of the Au dictates the photocatalytic performance of the NPs [29]. Briefly, the shape and size of the NPs is well-controlled, and their Au doping can be clearly identified by SEM and TEM (Fig. 1). The extiction spectra in Fig. 2 show that all the NPs have the most important absorption peak in the vicinity of 525 nm. There are two particularities to point out: The Au NPs have a much narrower LSPR than the absorption of the Cu$_2$O family, and the AuR@Cu$_2$O NPs possess an additional absorption peak near to 660 nm. It is worth pointing out that Cu$_2$O and the (Cu$_2$O + Au) curves in Fig. 2 strongly overlap. The Au NP sol was diluted with ultrapure water to obtain the same Au concentration in the mixture as that of the Au@Cu$_2$O sample. The differences
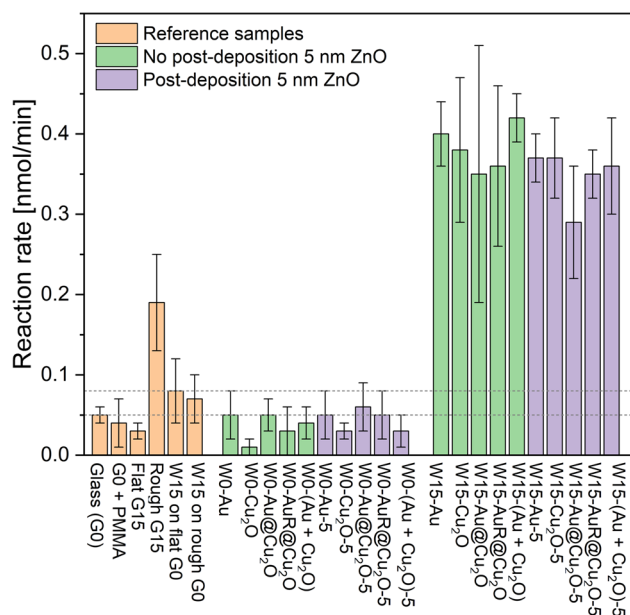
Figure 7 Graphical presentation of the average reaction rates after three consecutive photocatalytic tests on reference samples (orange), samples without post-deposition of 5 nm of ZnO (green), and samples with post-deposition of 5-nm ZnO (purple) after the deposition of the NPs.

but they cluster randomly upon drying. Despite the random clustering, the contribution from the LSPR can be clearly observed at 550 nm. The shape of transmittance curve of the Cu_2O NPs is in good agreement with their expected transmittance from the absorption curve reported in ref. [29]. The transmittance of $Au@Cu_2O$ NPs is almost perfectly parallel with that of the Cu_2O NPs but of lower value, due to the presence of Au nanograins on the surface of the Cu_2O octahedra. The transmittance of the $(Cu_2O + Au)$ sample is close to that of the $Au@Cu_2O$ sample in the range of 350–550 nm. From this wavelength, it starts to deviate from the $Au@Cu_2O$ curve toward the Cu_2O curve, and at 800 nm, the two curves overlap. At this wavelength, the transmittance of the Au sample reaches 100%.

In Fig. 3b, the transmittance of Au, Cu_2O, and $AuR@Cu_2O$ NPs is compared. In this case, the presence of the Au nanorods in the center of the Cu_2O octahedra has a much stronger and wavelength-dependent effect of the optical properties from 450 nm—where the LSPR of the Au NPs becomes observable, and the $Au–Cu_2O$ interaction manifests until 800 nm. The most important change in the transmittance amplitude of the $AuR@Cu_2O$ sample, of about 15–18% decrease is found in the region of 600–700 nm, which is associated with the presence of the Au nanorods and its interaction with the Cu_2O shell [29].

The comparison of the relative transmittance of the various samples from Cu_2O–Au NP family (Fig. 3) shows that the presence of Au modulates the properties of the Cu_2O NPs in a way which is dependent on the location and the shape of the Au and the kind of contact that is established between the Au and the Cu_2O. The differences of the various samples become significant at wavelengths larger than 550 nm, i.e., well in the visible spectrum.

It was reported recently that Cu_2O NPs suffer from severe charge recombination and insufficient light absorption, and their unsatisfactory photocatalytic performance can be improved by preparing designed core–shell structured $AuR@Cu_2O$ with preferentially edge-loaded Au NPs ($AuR@Cu_2O–Au(P)$) [43]. It was found that the light beyond the absorption range of Cu_2O particles can penetrate the shell (Cu_2O) and because it is utilized by the AuR core via the LSPR effect, hot electrons can be injected into the conduction band of Cu_2O for photocatalytic reactions. The investigation of the effect of illuminating light wavelength on the photodegradation of MO showed that the efficiency improved for $Cu_2O–Au_{(P)}$ and $Au_{(P)}@$

between the $(Cu_2O + Au)$ curve and that corresponding to the $Au@Cu_2O$ sample are an indication of the interaction between the Au nanograins and the Cu_2O carrier. Clearly, the decisive contribution in the total absorbance is that of Cu_2O.

The optical properties of the NPs were characterized in dry state, too, on glass substrates on which the same amount of NP sols was deposited as used for the wing samples. In Fig. 3a, the relative transmittance of the Au, Cu_2O, $Au@Cu_2O$, and $(Cu_2O + Au)$ NPs is compared with respect to clean glass. The Au NPs produce only a marginal decrease in the transmittance as their concentration is very low (0.015 mM in terms of Au^0) that would correspond to a continuous Au thin film of 0.4 nm in thickness. We recently investigated the effect of 5-nm- and 15-nm-thick Au thin films produced by physical vapor deposition (PVD) on glass and butterfly wings [54]. It was found that the 5-nm-thick Au film reduced the transmittance in the 500–600 nm spectral range by 30%. As a first approximation, one may estimate that a 12.5 times thinner film would decrease the transmission by 2.5%, which is an order of magnitude in good agreement with the measured data. Of course, the Au NPs of 20 nm in diameter do not constitute a continuous film of 0.4-nm thickness,

Cu_2O–$Au_{(P)}$-type nanoarchitectures, when illuminated at $\lambda \geq 420$ nm, but vanished when using light with $\lambda \geq 760$ nm. Similar results were obtained when using white LED illumination (400–800 nm) of octahedral and rhombic dodecahedral Cu_2O NPs [55]. The best-performing NPs were the rhombic dodecahedra, but even for these NPs, when the wavelengths shorter than 500 nm were filtered out, a much lower reaction rate was obtained than without filtering, indicating that the high reaction rate is due to wavelengths below 500 nm. In other words, the absorption and, therefore, the photogenerated charge carriers of Cu_2O are a crucial factor (Fig. 3).

The optical properties of the butterfly wings change with the different modifications (Fig. 4) as expected. The reflectance maxima are located in the spectral range from 350 to 450 nm. The removal of the wax layer causes a blue shift and increases in the reflectance maximum [49, 56], while the deposition of the 15-nm ZnO layer causes a reversed shift [14, 25, 27] to red. The ZnO layer is transparent in the visible but exhibits a high refractive index. First, it compensates for the decrease in the relative fraction of the high refractive index component of the chitinous photonic nanoarchitecture in the butterfly scales. With the increase in the deposited ZnO layer thickness, the reflectance maximum is shifted in the range of 400–600 nm [56], and the features present at smaller wavelength than 380 nm are masked by the ZnO absorption.

The effects of the NP deposition on wings with the wax removed (ETA50) wings and conformally coated with 15 nm of ZnO are shown in Figs. 5 and 6, respectively. The spectra measured before (black curves) and after the NP deposition (red curves), the relative reflectance (calculated as the ratio of reflectance after and before the NP deposition; blue curves) and the normalized absorbance of the MO (black dashed lines) are shown for each NP used. In agreement with Fig. 3, all samples exhibit a clear decrease in the amplitude of the reflectance maximum, except for the samples deposited only with Au NPs. This can be attributed to the absorption of the Cu_2O, which starts to decrease at wavelengths larger than 500 nm, in agreement with the data presented in Fig. 3 and literature reports [43, 55]. The relative reflectances in Figs. 5 and 6 (blue curves) show that the deposited NPs produce the redshift of the reflectance peak of all the biohybrid photonic nanoarchitectures, irrespective of the kind of the NPs, and presence/absence of the conformal ZnO coating of the wing. This indicates that the deposited NPs are

integrated into the photonic nanoarchitecture of the wing and tune their optical properties. It is not surprising that this tuning effect is stronger in the case of the wings without the conformal ZnO coating, as this coating already produced the alteration of the optical properties of the original photonic nanoarchitecture, also producing a redshift.

In Figs. 5 and 6, the gray shading indicates the spectral range in which one cannot expect important contributions to the photocatalytic process due to the transmittance edge of the cuvette. The filtering effect of the cuvette is more pronounced in the case of uncoated wings (Fig. 5), where even after the redshift caused by the NP deposition, almost half of the reflectance peaks fall in the shaded region. Another filtering effect that also has to be taken into account is the light absorption on the dissolved MO itself, reducing the intensity that reaches the wing surface [26]. The samples were uniformly fixed on the wall opposite to the illuminated wall of a glass cuvette of 1 cm in width, in other words, before reaching the photocatalytic surface, the light crossed 1 cm of MO dye solution. Adding these effects: the reduced transmission of the glass cuvette, the absence of the UV component from the illuminating light, and the absorption of the MO, it is not surprising that the apparent photocatalytic efficiency of some of the samples (Fig. 7) may appear very moderate. This moderate efficiency is not changed by the post-deposition of 5-nm ZnO after the deposition of the NPs. This thickness is insufficient for the formation of a continuous ZnO layer, as the formation of a continuous layer of ZnO is observed from 15 nm [14].

The optical micrographs of the NP-deposited wing samples, taken with a focus stacking microscope, are shown in Fig. S3. The deposited NPs show some clustering on the wing scales, which is to a certain degree dependent on the kind of the NPs used. The strongest clustering can be observed on the wing with AuR@Cu_2O NPs. This may be to a certain extent only an apparent effect, due to the strongest color contrast between the wing and the NPs, because of the additional absorption in the range of 600–700 nm. The post-deposition of 5-nm conformal ZnO following the NP deposition does not significantly modify the optical properties of the samples (Fig. S4).

The samples with 15-nm ZnO ad-layer show only a moderate photocatalytic performance (Fig. 7). The main reasons for this include the very low absorption of the ZnO in the visible, the transmittance window of the glass cuvette, and the low-intensity blue edge of

the light source (Fig. S7). One may estimate that only 12.6% of the total light power emitted by the source can be used by the ZnO thin film for dye decomposition. Altogether, it is very unlikely that the charge carriers released from the intra-band defects may have any contribution in the photodegradation process. An increase in the photodegradation on a roughened glass surface (Fig. 7) can be attributed to the increase in the effective surface area on which the dye can be adsorbed. A similar, but more reduced effect is observed for the wings conformally coated with 15-nm ZnO that is also attributed to the increased specific surface. However, the wing scales of *P. icarus* have a typical thickness in the order of 1 μm [44]; therefore, the mechanical roughening of the glass produces a significantly larger increase in the specific surface than the use of butterfly wing as substrate for the ZnO deposition. When the wings are fixed onto machined glass, the liquid PMMA fills the roughened surface, so it cannot influence the geometry of the wing. Therefore, the wings fixed onto flat and roughened glass after the deposition of 15 nm of ZnO have similar photocatalytic performance (Fig. 7).

The deposition of the NPs from Cu_2O–Au family does not cause a notable increase in the photocatalytic performance of the wing samples in the absence of the 15-nm ZnO coating. This is in agreement with our earlier findings for the case *P. icarus* wings and Cu_2O NPs deposited on clean wings, applied in the photocatalytic degradation of rhodamine B [25]. Post-deposition—after the deposition of the NPs—of 5 nm of ZnO does not change the photocatalytic activity of the samples. On average, some minor increase in the photocatalytic performance may be present, but the magnitude of this increase is far beyond that induced by the 15-nm ZnO coating of the wings prior to NP deposition. The value of the photocatalytic reaction rate for all types of NPs falls between that corresponding to the wings covered by 15-nm ZnO. This reduced photocatalytic activity can be attributed to the structural defects and the limited charge carrier mobility within the Cu_2O NPs [43].

In sharp contrast to all previous results, a dramatic change is observed when the NPs are deposited on wings with 15-nm conformal ZnO ad-layer. The photocatalytic activity of all samples increases between sixfold and eightfold as compared to the values of the photocatalytic reaction rate for the same NPs deposited on clean wings (Fig. 7). This result clearly shows that the increment can be attributed to the interaction of the NPs with the conformal ZnO coating of the wings.

Post-deposition of 5 nm of ZnO induces some changes in the activity of the samples, for most NPs reduces the standard deviation in the results of the three consecutive tests performed with the same samples (Fig. 7 and Table 2). This is attributed to the improvement of the electrical contact between the conformal ZnO layer and the NPs. However, compared to the rather uniform performance of the samples before the post-deposition of 5 nm of ZnO, after this processing step, some differences are accentuated between the samples prepared with different NPs (Fig. 7). The most significant decrease in the catalytic performance is observed for the $Au@Cu_2O$ NPs. This may be associated with at least partial encapsulation of the Au-decorated surface of the NPs by the post-deposited ZnO, so that the Au and the Cu_2O have reduced contact area with the dye solution. The $Au@Cu_2O$ sample had the weakest catalytic activity even before the post-deposition and exhibited the highest standard deviation in the results of the photocatalytic experiments.

The significant increase in the reaction rate is attributed to the heterojunction formation between the n-type semiconductor ZnO and the p-type semiconductor Cu_2O NPs. A somewhat different case is the formation of the junction between the ZnO layer and the Au NPs. It is worth to point out that both Cu_2O [57] and Au NPs [58, 59] are effective in charge separation when forming nanocomposite with ZnO, although in different ways.

It was reported that the addition of 5 wt% of Au to ZnO causes a significant increase in the visible range absorbance of the nanocomposite [60]. The addition of 10 wt% did not cause the doubling of the absorbance, this indicates that in this range of Au content, the effect does not scale linearly with the amount of the Au. The enhanced photocatalytic activity of the Au–ZnO nanocomposite was attributed to two factors: (i) the presence of the LSPR that causes additional light absorption in the visible and (ii) the presence of the Schottky junction that promotes charge separation and charge transfer [60]. Similar results were reported for Au/ZnO nanocomposites in the concentration range of 0.5–3 wt% of Au, again the increased absorbance in the visible region did not increase linearly with the Au concentration [61]. By using scavengers, it was found that $O_2{}^{-}$ and holes (h +) should be the two main active species of Au/ZnO in MO aqueous solution under visible light irradiation, and both of them play important roles for MO photodegradation process [61].

The combination of ZnO with Cu_2O has been investigated for solar cell applications [62, 63]. Both

Cu_2O/ZnO and ZnO/Cu_2O heterojunctions were fabricated by magnetron sputtering, and a significant forward–backward asymmetry was observed in the band alignments of Cu_2O/ZnO–ZnO/Cu_2O heterojunctions. This was attributed to the lattice distortion of the Cu_2O at the interface. Considering only the band alignments, the ZnO/Cu_2O structure has more advantages in photovoltaic applications than the Cu_2O/ZnO structure [62]. The ZnO–Cu_2O thin films prepared by electrodeposition show a high absorption between 300 and 650 nm with the absorption peak at 540 nm due to Cu_2O [63]. Results on Cu_2O layer grown to ZnO pillars for photodetectors show that upon illumination, the photogenerated electrons move from Cu_2O to the ZnO. The photodetector based on the p-type Cu_2O/n-type ZnO junction exhibits optimal performance, with photocurrents enhanced by a factor of 30 or 5000 over a single ZnO or Cu_2O-based photodetector (under 450-nm light illumination at 0 V) [64].

In photocatalytic experiments, the hybrid nanocomposite ZnO/Cu_2O was studied most frequently as ZnO decorated by Cu_2O [57, 65, 66]. ZnO nanorods or nanowires were decorated with Cu_2O NPs. The decoration by the Cu_2O NPs caused the extension of the ZnO absorption into the visible. While for a solar cell may be important from the side of which component the illuminating light falls on the device [62], for the photocatalytic nanohybrids, it may be important which is the major component of the nanohybrid [57, 65, 66]. The ZnO/Cu_2O hybrid nanocomposites exhibited much higher photocatalytic activity than either pure ZnO or Cu_2O. The enhancement of photocatalytic activity can be attributed to the n-ZnO/p-Cu_2O junction, which could improve the absorption and utilization ability of sunlight, favor charge transfer, and inhibit recombination of photoinduced electron–hole pairs [57]. In our experiments too, by combining two nanostructures, which present only a very moderate photocatalytic activity if separated (Fig. 7), a nanohybrid could be obtained in a simple way, showing synergy (Fig. 7).

Additionally to the effects of the junction formation, one can observe in Fig. 5 that both the reflectance peaks measured after the NP deposition (red curves) and the maximum of the relative reflectance of the samples (blue curves) fall to a good extent in the range of the absorption maximum of MO. So that the 1-cm light path through the aqueous MO solution causes the attenuation of the light. On the other hand, the deposition of the conformal ZnO redshifts the reflectance maximum of the bare wing (Fig. 4). Due to this,

after the deposition of the NPs (Fig. 6), both the red side reflectance maximum of the samples (red curves) and the maximum of the relative reflectance curves (blue curves) fall outside of the absorption of the MO solution, so that the attenuation of the light falling on the photocatalytic surface is close to negligible in this range, and the slow light effects due to the photonic nanoarchitecture [16, 17, 26] may contribute to the enhancement of the photodegradation process.

Under visible light illumination, the Cu_2O NP family on wings coated with 15 nm of conformal ZnO, the Cu_2O is the second most important component of the nanohybrid, so that the presence/absence and location of the Au on/in the Cu_2O NPs, opposite to only UV illumination in the absence of ZnO [29], the contribution of the Au NPs to photocatalysis is dominated by charge transfer processes at the ZnO/Cu_2O heterojunction. Since the Cu_2O is a much cheaper component than Au, and the results did not indicate leaching, it may be presumed that such hybrid nanoarchitectures can be used in wastewater remediation. First, the fraction of photocatalyst as compared with the volume of the treated samples is very low (an 8 mm in diameter surface vs. 20 ml of MO solution). Second, the components can be produced cheaply with standard materials science and chemical procedures, without using environmentally risky materials. Third, the hierarchical biotemplate used for anchoring the components of biohybrid nanocomposite can be produced cheaply and in environmentally safe way by herbivorous insects [13]. And fourth, the photocatalytic reaction does not need long induction time, so that a flow-through system may operate in natural sunlight, with a cheap plastic cover that allows the transmission of visible light.

Conclusions

Photocatalytic heteronanostructures were produced by integrating hybrid plasmonic Cu_2O–Au NPs into butterfly wings colored by photonic nanoarchitectures coated conformally by 15 nm of ZnO thin film using ALD. The photodegradation of methyl orange under visible light illumination in a glass cuvette was used to test the photocatalytic performance. It was found that the wings coated by ZnO and deposited by NPs surpass the catalytic efficiency by sixfold to eightfold of the wings not coated by ZnO. The significant increase in the photocatalytic efficiency is attributed: (i) to the formation of heterojunction between the n-ZnO and the p-Cu_2O, which produced

the separation of the photogenerated charge carriers; (ii) the extension of the light absorption of the ZnO into the visible by doping with the Cu_2O family NPs; and (iii) the red-shifting of the reflectance peak of the biological heteronanostructure by the ZnO deposition, in such a way that at the red edge of the reflectance peak, the slow light effects can contribute to the increased efficiency of the photodegradation of the methyl orange dye. The heterojunction formed between the ZnO and the Cu_2O dominated the photocatalytic process.

Both Cu_2O and ZnO are cheap, environmentally safe, and the biological template of the heteronanostructure can be produced in an environmentally safe way by breeding herbivorous insects. The consecutive repeating of the photocatalytic test under continuous magnetic stirring and the low values of standard deviation in the photocatalytic reaction rate show that the used NPs are anchored safely to the biohybrid substrate and will not be washed away if used in a flow-through system.

Acknowledgements

Author contributions

L.P.B. and J.S.P. helped in conceptualization; G.P., K.K., G.N., D.K., D.Z., J.S.P., and L.P.B. helped in data curation; G.P., K.K., G.N., and J.S.P. helped in formal analysis; G.P., D.Z., and L.P.B. helped in funding acquisition; G.P., K.K., G.N., D.K., and D.Z. worked in investigation; G.P., K.K., G.N., D.K., and Z.D. helped in methodology; L.P.B. worked in project administration; G.P., K.K., D.K., D.Z., and Z.B. helped in resources; L.P.B. and J.S.P. helped in supervision; G.P., K.K., G.N., J.S.P., and L.P.B. helped in validation; G.P., G.N., K.K., D.K., Z.D., and J.S.P. helped in visualization; L.P.B. contributed to writing—original draft; and G.P., K.K., G.N., D.K., D.Z., Z.B., and L.P.B. contributed to writing—review & editing.

Funding

Data availability

All relevant data analyzed during this study are included in this published article and its supplementary information files. Raw datasets used during the current study are available from the corresponding author on reasonable request.

Declarations

Conflict of interest   The authors declare no conflict of interest.

Supplementary Information   The online version contains supplementary material available at https://doi.org/10.1007/s10853-024-09764-5.

References

[1] Lu K (2019) Hybrid materials—a review on co-dispersion, processing, patterning, and properties. Int Mater Rev 65:463–501. https://doi.org/10.1080/09506608.2019.1653569

[2] Alshammari DA, El-Gawad HHA, Abdullah M, Manzoor S, El-Bahy ZM, Alzahrani HA, Raza N, Henaish AMA, Trukhanov S, Sayyed MI, Tishkevich D, Trukhanov A (2024) CuTe supported on graphitic carbon nitride nanocomposite as an effective electrocatalyst for oxidation of water in basic media. J Electroan Chem 953:118018. https://doi.org/10.1016/j.jelechem.2023.118018

[3] Karki S, Gohain MB, Yadav D, Ingole PG (2021) Nanocomposite and bio-nanocomposite polymeric materials/membranes development in energy and medical sector: a review. Int J Biol Macromol 193:2121–2139. https://doi.org/10.1016/j.ijbiomac.2021.11.044

[4] Zhu C, Tian L, Cheng W, Gu Z (2023) Bio-inspired photonic crystals: Tailoring the dielectric building blocks to control the light propagation. BMEMat. https://doi.org/10.1002/bmm2.12056

[5] Biró LP, Vigneron JP (2010) Photonic nanoarchitectures in butterflies and beetles: valuable sources for bioinspiration. Laser Photon Rev 5:27–51. https://doi.org/10.1002/lpor.200900018

[6] Bálint Z, Kertész K, Piszter G, Vértesy Z, Biró LP (2012) The well-tuned blues: the role of structural colours as optical signals in the species recognition of a local butterfly fauna (Lepidoptera: Lycaenidae: Polyommatinae). J R Soc Interface 9:1745–1756. https://doi.org/10.1098/rsif.2011.0854

[7] Wilts BD, Leertouwer HL, Stavenga DG (2008) Imaging scatterometry and microspectrophotometry of lycaenid butterfly wing scales with perforated multilayers. J R Soc Interface 6:S185–S192. https://doi.org/10.1098/rsif.2008.0299.focus

[8] Wilts BD, Apeleo Zubiri B, Klatt MA, Butz B, Fischer MG, Kelly ST, Spiecker E, Steiner U, Schröder-Turk GE (2017) Butterfly gyroid nanostructures as a time-frozen glimpse of intracellular membrane development. Sci Adv 3:e1603119. https://doi.org/10.1126/sciadv.1603119

[9] Kinoshita S, Yoshioka S, Kawagoe K (2002) Mechanisms of structural colour in the *Morpho* butterfly: cooperation of regularity and irregularity in an iridescent scale. Proc R Soc Lond B 269:1417–1421. https://doi.org/10.1098/rspb.2002.2019

[10] Piszter G, Kertész K, Bálint Z, Biró LP (2023) Wide-gamut structural colours on oakblue butterflies by naturally tuned photonic nanoarchitectures. R So Open Sci 10:221487. https://doi.org/10.1098/rsos.221487

[11] Bahrami M, Abenojar J, Martínez MÁ (2020) Recent progress in hybrid biocomposites: mechanical properties, water absorption, and flame retardancy. Materials 13:5145. https://doi.org/10.3390/ma13225145

[12] Czaplicki Z, Gliścińska E, Machnowski W (2021) Natural silk—an unusual fibre: origin, processing and world production. Fibres Text East Eur 29:22–28. https://doi.org/10.5604/01.3001.0014.9291

[13] Piszter G, Bálint Z, Kertész K, Szatmári L, Sramkó G, Biró LP (2023) Breeding *Polyommatus icarus* serves as a large-scale and environmentally friendly source of precisely tuned photonic nanoarchitectures. Insects 14:716. https://doi.org/10.3390/insects14080716

[14] Piszter G, Nagy G, Kertész K, Baji Z, Kovács K, Bálint Z, Horváth ZE, Pap JS, Biró LP (2023) Investigating the effect of reflectance tuning on photocatalytic dye degradation with biotemplated ZnO photonic nanoarchitectures based on *Morpho* butterfly wings. Materials 16:3584. https://doi.org/10.3390/ma16093584

[15] Mu Z, Zhao X, Xie Z, Zhao Y, Zhong Q, Bo L, Gu Z (2013) In situ synthesis of gold nanoparticles (AuNPs) in butterfly wings for surface enhanced Raman spectroscopy (SERS). J Mater Chem B 1:1607–1613. https://doi.org/10.1039/c3tb00500c

[16] Liu J, Zhao H, Wu M, Van der Schueren B, Li Y, Deparis O, Ye J, Ozin GA, Hasan T, Su B (2017) Slow photons for photocatalysis and photovoltaics. Adv Mater 29:1–21. https://doi.org/10.1002/adma.201605349

[17] Lonergan A, O'Dwyer C (2022) Many facets of photonic crystals: from optics and sensors to energy storage and photocatalysis. Adv Mater Technol 8:2201410. https://doi.org/10.1002/admt.202201410

[18] Rodríguez RE, Agarwal SP, An S, Kazyak E, Das D, Shang W, Skye R, Deng T, Dasgupta NP (2018) Biotemplated *Morpho* butterfly wings for tunable structurally colored photocatalysts. ACS Appl Mater Interfaces 10:4614–4621. https://doi.org/10.1021/acsami.7b14383

[19] Chen Z, Zhang Z, Wang Y, Xu D, Zhao Y (2021) Butterfly inspired functional materials. Mater Sci Eng R 144:100605. https://doi.org/10.1016/j.mser.2020.100605

[20] Liu Z, Leow WR, Chen X (2018) Bio-inspired plasmonic photocatalysts. Small Methods 3:1–14. https://doi.org/10.1002/smtd.201800295

[21] Barber J, Tran PD (2013) From natural to artificial photosynthesis. J R Soc Interface 10:20120984. https://doi.org/10.1098/rsif.2012.0984

[22] Lang X, Chen X, Zhao J (2014) Heterogeneous visible light photocatalysis for selective organic transformations. Chem Soc Rev 43:473–486. https://doi.org/10.1039/C3CS60188A

[23] Yang L, Fan D, Li Z, Cheng Y, Yang X, Zhang T (2022) A review on the bioinspired photocatalysts and photocatalytic systems. Adv Sustain Syst 6:1–18. https://doi.org/10.1002/adsu.202100477

[24] Zhu M, Zhang H, Favier SWL, Zhao Y, Guo H, Du Z (2022) A general strategy towards controllable replication of butterfly wings for robust light photocatalysis. J Mater Sci Technol 105:286–292. https://doi.org/10.1016/j.jmst.2021.07.035

[25] Piszter G, Kertész K, Nagy G, Baji Z, Endre Horváth Z, Bálint Z, Sándor Pap J, Péter Biró L (2022) Spectral tuning of biotemplated ZnO photonic nanoarchitectures for photocatalytic applications. R Soc Open Sci 9:220090. https://doi.org/10.1098/rsos.220090

[26] Lim SY, Hedrich C, Jiang L, Law CS, Chirumamilla M, Abell AD, Blick RH, Zierold R, Santos A (2021) Harnessing slow light in optoelectronically engineered nanoporous photonic crystals for visible light-enhanced photocatalysis. ACS Catal 11:12947–12962. https://doi.org/10.1021/acscatal.1c03320

[27] Piszter G, Kertész K, Kovács D, Zámbó D, Baji Z, Illés L, Nagy G, Pap JS, Bálint Z, Biró LP (2022) Spectral engineering of hybrid biotemplated photonic/photocatalytic nanoarchitectures. Nanomaterials 12:4490. https://doi.org/10.3390/nano12244490

[28] Yuan G, Hsia C, Lin Z, Chiang C, Chiang Y, Huang MH (2016) Highly facet-dependent photocatalytic properties of Cu_2O crystals established through the formation of Au-decorated Cu_2O heterostructures. Chem A Eur J 22:12548–12556. https://doi.org/10.1002/chem.201602173

[29] Kovács D, Deák A, Radnóczi GZ, Horváth ZE, Sulyok A, Schiller R, Czömpöly O, Zámbó D (2023) Position of gold dictates the photophysical and photocatalytic properties of Cu_2O in Cu_2O/Au multicomponent nanoparticles. J Mater Chem C 11:8796–8807. https://doi.org/10.1039/D3TC01213A

[30] Kuo C-H, Huang MH (2010) Morphologically controlled synthesis of Cu_2O nanocrystals and their properties. Nano Today 5:106–116. https://doi.org/10.1016/j.nantod.2010.02.001

[31] Xiong L, Huaqing Y, Ba X, Zhang W, Ying Y (2014) Cu_2O-based nanocomposites for environmental protection. In: Kharisov BI, Kharissova OV, Rasika Dias HV (eds) Nanomaterials for environmental protection. Wiley, New Jersey, pp 41–70. https://doi.org/10.1002/9781118845530.ch3

[32] Yang Y-C, Wang H-J, Whang J, Huang J-S, Lyu L-M, Lin P-H, Gwo S, Huang MH (2014) Facet-dependent optical properties of polyhedral Au–Cu_2O core–shell nanocrystals. Nanoscale 6:4316–4324. https://doi.org/10.1039/c3nr06293g

[33] Sawant SS, Bhagwat AD, Mahajan CM (2016) Synthesis of cuprous oxide (Cu^2O) nanoparticles—a review. J Nano-Electron Phys 8:01035-1-01035–5. https://doi.org/10.21272/jnep.8(1).01035

[34] Yu Y, Zhang Q, Hao L, Huo H, Li M, Liu X, Wang S, Min D (2022) Heterogeneous Cu_2O–Au nanocatalyst anchored on wood and its insight for synergistic photodegradation of organic pollutants. Environ Res 215:114298. https://doi.org/10.1016/j.envres.2022.114298

[35] Prakruthi K, Ujwal MP, Yashas SR, Mahesh B, Kumara Swamy N, Shivaraju HP (2021) Recent advances in photocatalytic remediation of emerging organic pollutants using semiconducting metal oxides: an overview. Environ Sci Pollut Res 29:4930–4957. https://doi.org/10.1007/s11356-021-17361-1

[36] Wang W-C, Lyu L-M, Huang MH (2011) Investigation of the effects of polyhedral gold nanocrystal morphology and facets on the formation of Au–Cu_2O core-shell heterostructures. Chem Mater 23:2677–2684. https://doi.org/10.1021/cm200708q

[37] Pang M, Wang Q, Zeng HC (2012) Self-generated etchant for synthetic sculpturing of Cu_2O-Au, Cu_2O@Au, Au/Cu_2O, and 3D-Au nanostructures. Chem A Eur J 18:14605–14609. https://doi.org/10.1002/chem.201202765

[38] Huang MH, Rej S, Chiu C (2015) Facet-dependent optical properties revealed through investigation of polyhedral Au–Cu_2O and bimetallic core-shell nanocrystals. Small 11:2716–2726. https://doi.org/10.1002/smll.201403542

[39] Zakria HS, Othman MHD, Kamaludin R, Sheikh Abdul Kadir SH, Kurniawan TA, Jilani A (2021) Immobilization techniques of a photocatalyst into and onto a polymer membrane for photocatalytic activity. RSC Adv 11:6985–7014. https://doi.org/10.1039/D0RA10964A

[40] Han Y, Meng Z, Wu Y, Zhang S, Wu S (2021) Structural colored fabrics with brilliant colors, low angle dependence, and high color fastness based on the Mie scattering of Cu_2O spheres. ACS Appl Mater Interfaces 13:57796–57802. https://doi.org/10.1021/acsami.1c17288

[41] Sugimoto H, Fujii M (2021) Colloidal Mie resonators for all-dielectric metaoptics. Adv Photon Res 2:2000111. https://doi.org/10.1002/adpr.202000111

[42] Zhang S, Jiang R, Xie Y, Ruan Q, Yang B, Wang J, Lin H (2015) Colloidal moderate-refractive-index Cu$_2$O nanospheres as visible-region nanoantennas with electromagnetic resonance and directional light-scattering properties. Adv Mater 27:7432–7439. https://doi.org/10.1002/adma.201502917

[43] Yu X, Liu X, Wang B, Meng Q, Sun S, Tang Y, Zhao K (2020) An LSPR-based "push–pull" synergetic effect for the enhanced photocatalytic performance of a gold nanorod@cuprous oxide-gold nanoparticle ternary composite. Nanoscale 12:1912–1920. https://doi.org/10.1039/C9NR08808C

[44] Kertész K, Piszter G, Horváth ZE, Bálint Z, Biró LP (2017) Changes in structural and pigmentary colours in response to cold stress in *Polyommatus icarus* butterflies. Sci Rep 7:1118. https://doi.org/10.1038/s41598-017-01273-7

[45] Kertész K, Piszter G, Bálint Z, Biró LP (2019) Biogeographical patterns in the structural blue of male *Polyommatus icarus* butterflies. Sci Rep 9:2338. https://doi.org/10.1038/s41598-019-38827-w

[46] Turkevich J, Stevenson PC, Hillier J (1951) A study of the nucleation and growth processes in the synthesis of colloidal gold. Discuss Faraday Soc 11:55–75. https://doi.org/10.1039/DF9511100055

[47] Zámbó D, Radnóczi GZ, Deák A (2015) Preparation of compact nanoparticle clusters from polyethylene glycol-coated gold nanoparticles by fine-tuning colloidal interactions. Langmuir 31:2662–2668. https://doi.org/10.1021/la504600j

[48] Scarabelli L, Sánchez-Iglesias A, Pérez-Juste J, Liz-Marzán LM (2015) A "tips and tricks" practical guide to the synthesis of gold nanorods. J Phys Chem Lett 6:4270–4279. https://doi.org/10.1021/acs.jpclett.5b02123

[49] Piszter G, Kertész K, Kovács D, Zámbó D, Cadena A, Kamarás K, Biró LP (2024) Integrating Cu$_2$O colloidal Mie resonators in structurally colored butterfly wings for bio-nanohybrid photonic applications. Nanomaterials, (under review)

[50] Liu J, Ma Y, Shao J, Zhang S, Chen Y (2018) Ultra-tall sub-wavelength gold nano pillars for high sensitive LSPR sensors. Microelectron Eng 196:7–12. https://doi.org/10.1016/j.mee.2018.04.007

[51] Garcia MA, de la Venta J, Crespo P, Lopis J, Penadés S, Fernández A, Hernando A (2005) Surface plasmon resonance of capped Au nanoparticles. Phys Rev B 72:241403. https://doi.org/10.1103/PhysRevB.72.241403

[52] Walsh GF, Negro LD (2013) Engineering plasmon-enhanced Au light emission with planar arrays of nanoparticles. Nano Lett 13:786–792. https://doi.org/10.1021/nl304523v

[53] Fu S, Chen J, Han H, Wang W, Shi H, Fu J, Jia Y (2019) ZnO@Au@Cu$_2$O nanotube arrays as efficient visible-light-driven photoelectrode. J Alloys Compd 799:183–192. https://doi.org/10.1016/j.jallcom.2019.05.340

[54] Kertész K, Piszter G, Beck A, Horváth A, Nagy G, Molnár G, Radnóczi GZ, Horváth ZE, Illés L, Biró LP (2023) Hybrid bio-nanocomposites by integrating nanoscale Au in butterfly scales colored by photonic nanoarchitectures. Photonics 10:1275. https://doi.org/10.3390/photonics10111275

[55] Su Y, Nathan A, Ma H, Wang H (2016) Precise control of Cu$_2$O nanostructures and LED-assisted photocatalysis. RSC Adv 6:78181–78186. https://doi.org/10.1039/C6RA19037E

[56] Kertész K, Baji Z, Deák A, Piszter G, Rázga Z, Bálint Z, Biró LP (2021) Additive and subtractive modification of butterfly wing structural colors. Colloids Interface Sci Commun 40:100346. https://doi.org/10.1016/j.colcom.2020.100346

[57] He Z, Xia Y, Tang B, Jiang X, Su J (2016) Fabrication and photocatalytic property of ZnO/Cu$_2$O core-shell nanocomposites. Mater Lett 184:148–151. https://doi.org/10.1016/j.matlet.2016.08.020

[58] Kim K-J, Kreider PB, Chang C-H, Park C-M, Ahn H-G (2013) Visible-light-sensitive nanoscale Au–ZnO photocatalysts. J Nanopart Res 15:1606. https://doi.org/10.1007/s11051-013-1606-5

[59] Meng X, Zong P, Wang L, Yang F, Hou W, Zhang S, Li B, Guo Z, Liu S, Zuo G, Du Y, Wang T, Roy VAL (2020) Au-nanoparticle-supported ZnO as highly efficient photocatalyst for H$_2$O$_2$ production. Catal Commun 134:105860. https://doi.org/10.1016/j.catcom.2019.105860

[60] Mondal C, Pal J, Ganguly M, Sinha AK, Jana J, Pal T (2014) A one pot synthesis of Au–ZnO nanocomposites for plasmon-enhanced sunlight driven photocatalytic activity. New J Chem 38:2999–3005. https://doi.org/10.1039/c4nj00227j

[61] Liu T, Chen W, Hua Y, Liu X (2017) Au/ZnO nanoarchitectures with Au as both supporter and antenna of visible-light. Appl Surf Sci 392:616–623. https://doi.org/10.1016/j.apsusc.2016.09.033

[62] Yang M, Zhu L, Li Y, Cao L, Guo Y (2013) Asymmetric interface band alignments of Cu$_2$O/ZnO and ZnO/Cu$_2$O heterojunctions. J Alloys Compd 578:143–147. https://doi.org/10.1016/j.jallcom.2013.05.033

[63] Fujimoto K, Oku T, Akiyama T (2013) Fabrication and characterization of ZnO/Cu$_2$O solar cells prepared by electrodeposition. Appl Phys Express 6:086503. https://doi.org/10.7567/APEX.6.086503

[64] Zhong S, Xiong D, Zhang B, Yang X, Yang T, Tian G, Zhang H, Yang W, Deng W (2022) Structurally unraveling the photocarrier behavior of Cu_2O/ZnO heterojunction photodetectors. ACS Photon 9:268–274. https://doi.org/10.1021/acsphotonics.1c01490

[65] Wei A, Xiong L, Sun L, Liu Y-J, Li W-W (2013) CuO nanoparticle modified ZnO nanorods with improved photocatalytic activity. Chin Phys Lett 30:046202. https://doi.org/10.1088/0256-307X/30/4/046202

[66] Chang Y-H, Chiang M-Y, Chang J-H, Lin H-N (2015) Enhanced visible light photocatalysis of cuprous oxide nanoparticle modified zinc oxide nanowires. Mater Lett 138:85–88. https://doi.org/10.1016/j.matlet.2014.09.098